Associative ionization in collisions between two Na(3P) atoms

J. Huennekens* and A. Gallagher†

*Joint Institute for Laboratory Astrophysics, University of Colorado
and National Bureau of Standards, Boulder, Colorado 80309*

(Received 28 March 1983)

We have measured the rate coefficient [$k = 5.6 \times 10^{-12}$ cm^3/s ($\pm 37\%$)] for associative ionization occurring in collisions between two Na(3P) atoms, by measuring the current resulting from excitation of Na vapor by cw-laser radiation. The major source of uncertainty in measurements of this type is in the determination of the number density and spatial distribution of excited atoms. Here we have measured the excited-atom density by three methods, and we have studied the spatial distribution of excited atoms in detail. Our rate coefficient at $T \sim 650$ K is compared to other experimental results.

I. INTRODUCTION

Associative ionization (AI) occurring in collisions between two excited atoms can be important in many situations, and is a sensitive test of the excited electronic states of the diatomic molecule. Associative ionization is important in studies of flames and electrical discharges, and in astrophysical problems such as molecule formation, ionization equilibria, and radiative transfer. Additionally, AI is one possible method for achieving laser isotope separation.

Large excited-atom populations often exist in laser-excited radiation vapors, and AI due to collisions of two excited atoms may be significant in models of such environments. An important example of this is in laser-driven ionization[1,2] in which very efficient and almost complete ionization is observed in high-density metal vapors illuminated by resonance radiation. Measures[3] has proposed that the runaway ionization results from atoms colliding with superelastically heated electrons. However, models of this ionization process all require some mechanism to produce the initial or "seed" electrons. In sodium vapor, the most likely seeding mechanisms involve multistep ionization of Na$_2$ and collisions between two excited atoms. Ionization can occur directly by associative ionization

$$\text{Na}(3P) + \text{Na}(3P) \xrightarrow[k_{AI}]{} \text{Na}_2^+ + e^- , \qquad (1)$$
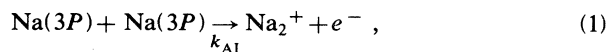
or indirectly by photoionization or collisional ionization of higher levels populated through excited-atom—excited-atom excitation transfer collisions

$$\text{Na}(3P) + \text{Na}(3P) \xrightarrow[k_{nL}]{} \text{Na}(nL) + \text{Na}(3S) . \qquad (2)$$
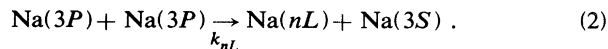
Here k_{AI} and k_{nL} are the rate coefficients for AI and excitation transfer, respectively (see Fig. 1). Analogous processes may prove to be important seeding mechanisms in the laser-driven ionization of other group-I and group-II elements. Reliable rate coefficients for both (1) and (2) are needed to interpret the laser-driven ionization and other experiments involving excited Na atoms.

The major experimental difficulty in determining k_{AI} and k_{nL} is the accurate evaluation of the excited-atom density and spatial distribution. Previous measurements[6-10] of both processes (1) and (2) have generally made unverified assumptions about the 3P-atom density and distribution, and we believe that this is the primary cause of the orders-of-magnitude differences in reported rate coefficients. We have recently reported measurements of the rate coefficients k_{4D} and k_{5S} in which the excited-atom density and spatial distribution, following excitation by high-power pulsed-laser radiation, were directly measured.[11] In the present measurements we have used excitation by cw-laser (low-power) radiation to avoid several extraneous causes of ionization that can occur under pulsed-laser (high-power) radiation conditions. Some additional observations using pulsed-laser radiation are discussed in Sec. V. In the present study of Na(3P)-Na(3P)
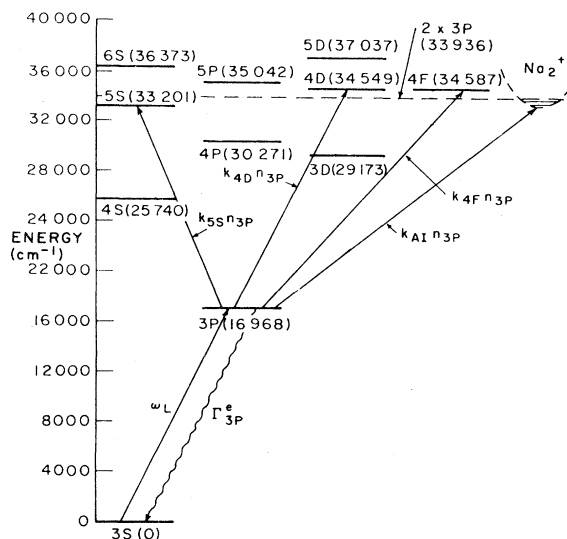

FIG. 1. Sodium energy levels involved in excited-atom—excited-atom collisional processes. The energy of two Na(3P) atoms is indicated by the dashed line; all other energies are Na(nL) + Na(3S) relative to Na(3S) + Na(3S). Energies are given in cm^{-1} (from Ref. 4). Na$_2^+$ potential from Ref. 5.

AI we have used three different techniques for determining the excited-atom density resulting from cw-laser excitation. We therefore believe that the measurement reported here has removed this major cause of uncertainty in previous measurements of k_{AI}.

As seen in Fig. 1, the bottom of the Na_2^+ potential well lies very near twice the $3P$-level energy. Since $Na(3P) + Na(3P)$ connects to many electronic states of Na_2, it is therefore likely that some of these cross the Na_2^+ potential at or below the $3P + 3P$ energy, and as a result k_{AI} may be fairly large.

The number of electrons, and Na_2^+ ions, produced by process (1) per unit time and per unit volume in the experimental cell is given by

$$\dot{n}_e(x,y,z) = k_{AI}[n_{3P}(x,y,z)]^2 . \tag{3}$$

If all electrons produced in a volume V by this mechanism are collected, the resultant current i will be given by

$$i = ek_{AI} \int \int \int dx\, dy\, dz [n_{3P}(x,y,z)]^2 , \tag{4}$$

where the integrals extend over the volume V. A measurement of i, combined with a knowledge of the $3P$-atom density and spatial distribution, will therefore yield the rate coefficient k_{AI}. As stated previously, it is the determination of $n_{3P}(x,y,z)$ that presents the major difficulties and introduces the largest source of uncertainty in the results.

II. EXPERIMENT

Figure 2 is a block diagram of the experimental arrangement, including a horizontal cross section of the cell and a coordinate system, with origin at the center of the cell and y axis out of the paper. A cross section of the cell in the x-y plane is shown in Fig. 3. The cell is a 5-cm stainless-steel block drilled out to make a cross and vacu-

FIG. 3. x-y cross section of the cell interior (see also Fig. 2). Laser beam propagates out of the page (along the z axis). Light is detected perpendicular to the sapphire-rod surface (in the x direction). Spectrometer slit is oriented along y collecting light from a thin volume at $z = 0$ of 5-mm height (the region between the dashed lines). Also shown are the x and y distributions of the excited atoms $\phi(x)$ and $Y(y)$. Dashed x distribution curve is the laser spatial profile $I(x)$, while the dotted x distribution curve is the infinite-slab fundamental mode distribution $n_0(x)$ from Ref. 12. Solid curve is $\phi_{ss}(x)$, obtained from Eqs. (7) and (8) using the first four even eigenmodes [see Eq. (6) and Ref. 12]. $Y(y)$ was obtained from measurements of the $3P$ fluorescence as a function of y. For $Y(y)$ shown here [Na] $= 2.07 \times 10^{14}$ cm^{-3} and the laser was tuned near the D_2 frequency.
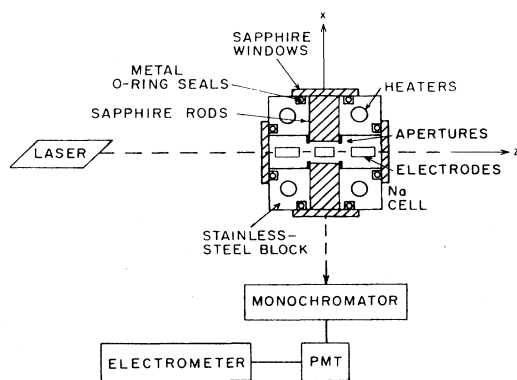

FIG. 2. Diagram of the apparatus. Cross section of the cell mid-plane is shown; the electrodes are below this plane, as shown in Fig. 3. Na is confined to the cross bored through the stainless-steel block, but is excluded from the two arms containing sapphire rods. Origin of the x,y,z axes shown is in the center of the oven, here and in Fig. 3. Stainless-steel block is directly heated and sits inside an insulating firebrick oven with quartz windows to decrease cooling of the cell's sapphire windows. PMT is the photomultiplier.
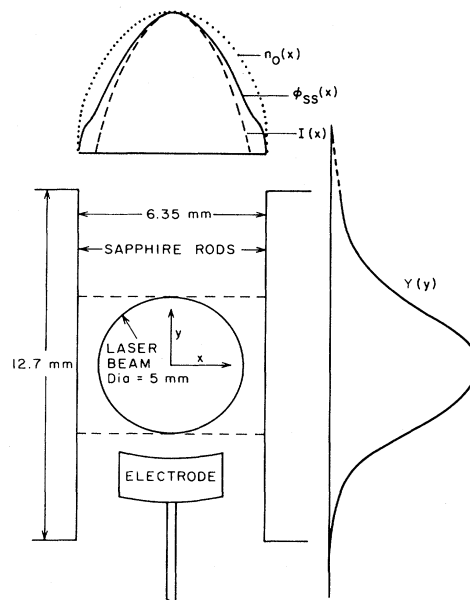
um sealed with metal O-rings to sapphire windows. As indicated, two arms of the cross contain sapphire rods which simplify the cell geometry. Two stainless-steel apertures are held at ground potential and effectively divide the cell into three regions in the z direction (Fig. 2). This cell has been described previously in Refs. 11, 13, and 14. For the present experiment, a current collecting electrode was inserted into each of the three regions defined by the apertures. Electrical connections to the electrodes were made using ceramic feed-throughs which were maintained at the oven temperature of ~ 380 °C. Guard rings of silver paint were made around each electrode on the feed-throughs and wherever insulators contacted the cell body. The guard rings were maintained at the electrode potential to reduce surface currents, due to the Na vapor, from the electrodes to the grounded cell body.

Sodium vapor pressure in the cell was controlled by the temperature of a sidearm, which was stabilized at typically 25–100 °C below the cell temperature. Vapor pressure as a function of temperature reading was calibrated at low density by measurement of k_0, the line-center absorption coefficient, and at high density by measurement of k_v, the

wing absorption coefficient, combined with an independent measurement of the self-broadening rate for the resonance lines (see Refs. 14 and 15).

The vapor was excited with a single-mode cw dye laser with $\sim$20-mW power in a 0.5-cm-diam beam. The laser frequency was near the D_2 line $(3S_{1/2} \rightarrow 3P_{3/2})$ and the detuning was set such that $\sim$10% of the incident intensity was transmitted. Typically, detunings were in the range 4—20 GHz. At these intensities and detunings, optical-pumping effects are expected to be negligible although the experimental results are in any case insensitive to such effects.

Fluorescence from the decay of atoms in the $3P$, $4D$, and $5S$ levels was observed at right angles to the laser beam with a $\frac{3}{4}$-m double monochromator and a photomultiplier with an S-20 cathode response. Photomultiplier currents were measured by an electrometer and displayed on a chart recorder. Ionization currents from the electrodes were measured directly by an electrometer for absolute rate coefficient determinations, although these signals had to be corrected for the background surface currents which were measured by blocking the laser. A beam chopper and lock-in detection were used to obtain the laser power, laser detuning, and electrode voltage dependences of the ionization signals which will be discussed in Sec. IV.

III. DETERMINATION OF THE EXCITED-ATOM DENSITY AND SPATIAL DISTRIBUTION

As noted in the Introduction, the signal is proportional to a volume integral of n_{3P}^2 [Eq. (4)], and the distribution and size of n_{3P} is crucial. Consequently, we have measured n_{3P} by three different techniques and have carefully considered its spatial distribution.

Since cell geometry plays an important role in the experiment, we have provided, in Fig. 3, a detailed cross section in the x-y plane through the cell center. The plane of this cross section is indicated in Fig. 2. The observation depends on the excited-atom density in the central region between the apertures in Fig. 2. This is predominantly a 6.35-mm-wide slab between the ends of the 12.7-mm sapphire-rod "windows." Owing to radiation diffusion, the excited-atom density is spread out from the initially excited (5-mm-diam) cyclindrical region defined by the laser beam. In order to obtain this resultant excited-state distribution, we essentially use slab-geometry radiation diffusion theory for the x dependence, measured fluorescence versus y for the y dependence, and known laser power variation for the z dependence (see Figs. 2 and 3 for the definition of coordinates).

To put this on a quantitative basis we take $n_{3P}(x,y,z)$ to be separable in the coordinates, i.e., that

$$n_{3P}(x,y,z) \equiv n_{3P}(0,0,0)\phi(x)Y(y)Z(z) , \qquad (5)$$

where the dimensionless functions $\phi(x)$, $Y(y)$, and $Z(z)$ are defined such that $\phi(0)=Y(0)=Z(0)=1$, and the origin is taken as the cell geometric center. Departures from this assumed separation of variables are relatively minor, whereas this yields major simplification to the calculation

and causes minor ($<10\%$) uncertainties compared to others described below.

The cell and laser geometry are essentially independent of z and the laser power varies gradually with z (typically by 40% in the central chamber of the cell between the apertures in Fig. 2). Thus even with radiation diffusion the z dependence of the excited-atom density is essentially proportional to the laser-beam power, which varies as $e^{-k_\nu z}$. The laser attenuation factor k_ν was calculated from the ratio of laser-beam power before and after traversing the cell, with the laser tuned on and off resonance to correct for window attenuation. Owing to the separation of x and y variables in Eq. (5) the radiation emitted perpendicular to the window at y is proportional to $Y(y)$, in spite of radiation trapping. Thus $Y(y)$ was measured by observing the $3P$ fluorescence as a function of y (see Ref. 15). A typical curve of $Y(y)$ for [Na] $=2.07\times10^{14}$ cm^{-3} is shown in Fig. 3. Spatial resolution for this measurement was 1.3 mm, compared to $\sim$6-mm half-width of $Y(y)$. The size of the windows did not permit measurement of $Y(y)$ beyond $y=\pm6.3$ mm although Na vapor is present in these regions (see Fig. 3). Extrapolations of $Y(y)$ in these regions are shown in Fig. 3 by dashed lines. [Note that the presence of the electrode introduces an asymmetry into $Y(y)$ and a breakdown in the separability approximation (5). However, as this region is a small fraction of the total volume, process (1) is proportional to n_{3P}^2 and n_{3P} here is relatively small, the perturbation to the geometry introduced by the electrode introduces minor uncertainty in the results.] The procedure of extrapolating $Y(y)$ beyond the window edges, as shown in Fig. 3, has been described previously in Refs. 14 and 15. In the present experiment these extrapolations introduce very minor uncertainty into k_{AI} since the ion signal is proportional to $[Y(y)]^2$ which is very small beyond the window edges.

$\phi(x)$ was determined from radiation trapping theory, rather than being measured. According to Holstein's theory[16] of radiation trapping, the excited-atom spatial distribution as a function of time following pulsed excitation at $t=0$, by radiation spatially distributed as $I(x)$, can be expanded in slab-geometry eigenmodes as

$$n_{3P}(x,t) = \sum_i a_i n_i(x)e^{-\beta_i t} , \qquad (6)$$

where in the absence of saturation

$$a_i = \int I(x)n_i(x)dx . \qquad (7)$$

The first eigenstate $n_0(x)$ is called the fundamental mode and corresponds to the slowest decaying eigenvalue β_0. (It is also customary to define an effective escape factor $g_i \equiv \beta_i /\Gamma_N$, where Γ_N is the spontaneous emission rate.) In Ref. 11, where pulsed-laser excitation was used, we measured rate coefficients in the late time following the pulse, when all but the fundamental mode had decayed away. Thus the infinite-slab fundamental-mode distribution $n_0(x)$ normalized to 1 at $x=0$, accurately represented $\phi(x)$ for that measurement. In the present cw-laser-excitation experiment, higher eigenmodes are present and must be included. The steady-state $\phi(x)$ distribution is ob-

tained by integration of Eq. (6) over excitation times with a constant excitation rate. The result, normalized to $\phi(0) = 1$, is

$$\phi_{ss}(x) = \sum \beta_i^{-1} a_i n_i(x) \Big/ \sum \beta_i^{-1} a_i n_i(0) , \qquad (8)$$

where a_i is given by Eq. (7), in which $I(x)$ is now the cw-laser intensity. In order to produce primarily the fundamental mode, we have used a 5-mm beam diameter which nearly fills the 6.3-mm-wide region between the sapphire rods. Figure 3 shows the laser-intensity profile $I(x) = \int dy\, I(x,y)$ measured at the cell entrance (dashed line), $\phi_{ss}(x)$ (solid line), and the infinite-slab fundamental-mode spatial distribution $n_0(x)$ (dotted line). Here all three distributions are normalized to one at $x = 0$. To obtain this $\phi_{ss}(x)$ we have used $n_i(x)$ and β_i calculated by van Trigt,[12] whose calculations are based on Holstein's theory. The odd-numbered modes are asymmetric and have zero amplitude for our symmetric $I(x)$. The $\phi_{ss}(x)$ in Fig. 3 was obtained by truncating the sums in (7) and (8) after the fourth ($i = 6$) even term. For comparison, truncating after the second ($i = 2$) even term yields $\phi_{ss}(x)$ within 0.03 of that shown at all x. This $\phi_{ss}(x)$ is the best representation of the actual $\phi(x)$. The $I(x)$ and $n_0(x)$ curves put extreme bounds on the possible $\phi(x)$, since $\phi(x) = I(x)$ if there were no radiation diffusion and $\phi(x) = n_0(x)$ is the broadest possible distribution. Thus these extreme bounds yield convenient estimates of the effect of different distributions on the various integrals. Owing to surface reflections, uncertainty in $I(x)$, and the absence of a truly infinite-slab geometry, some uncertainty in $\phi(x)$ still remains.

Three independent methods were used to obtain $n_{3P}(0,0,0)$. First and most straightforward, the total number of excited atoms in the cell was calculated from the measured laser power absorbed $P(z)dz$, which must equal the number of excited atoms in z to $z + dz$ multiplied by the photon energy and the effective radiative rate $\Gamma_{eff} \equiv \Gamma_N g$. Then g was calculated from application of Eqs. (6)—(8), and the spatial distribution functions $\phi(x)$ and $Y(y)$ were used to obtain $n_{3P}(0,0,0)$. This technique and associated uncertainties are discussed in Appendix A.
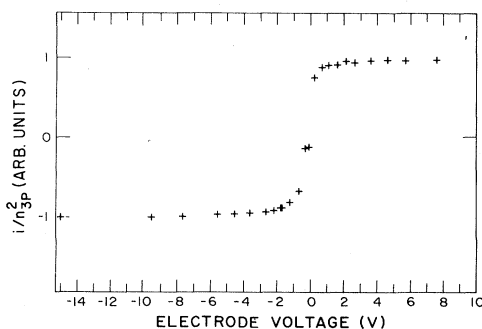

FIG. 4. Current vs electrode voltage. Ion signals have been divided by the square of the D_1 fluorescence signal which corrects for laser power and frequency drifts. Background surface currents were eliminated by chopping the laser and using lock-in detection. Laser was detuned ~ 5.2 GHz to the blue of the D_2 line. [Na] $\sim 6.8 \times 10^{13}$ cm^{-3}.

Second, we determined $n_{3P}(0,0,0)$ using the total 3P-atom fluorescence intensity, which is calibrated using an absolute 3P density determination described in Ref. 11, based on a change in resonance-line absorption following pulsed excitation. Details of this technique are given in Appendix B. Finally, the ratio of $5S \rightarrow 3P$ fluorescence, due to process (2), to $3P \rightarrow 3S$ fluorescence intensity is proportional to $n_{3P}(0,0,0)k_{5S}$. Since we have previously[11] measured the rate coefficient k_{5S} for process (2), we used this intensity ratio to calculate $n_{3P}(0,0,0)$ in the present experiment. Details of this method, which is basically a consistency check between k_{5S} from Ref. 11 and k_{AI} obtained here, are provided in Appendix C.

In each of these three methods, fairly large uncertainties in $n_{3P}(0,0,0)$ occur due to lack of accurate knowledge of $\phi(x)$. However, in all cases, an optimum value is obtained using $\phi_{ss}(x)$ and the uncertainty in this can be estimated from the maximum and minimum value of $n_{3P}(0,0,0)$ obtained by using the limiting cases $\phi(x) = I(x)$ and $n_0(x)$ shown in Fig. 3. We note that in all cases, the three determinations of $n_{3P}(0,0,0)$ agree within their uncertainties. The various contributions to the uncertainty in k_{AI} will be discussed in Sec. IV.

IV. RESULTS

All three electrodes and guard rings were maintained at the same voltage and the two grounded apertures guaranteed that each electrode collected ions or electrons produced almost exclusively in its own chamber (see Fig. 2). The electrode current in the central chamber was measured as a function of several parameters in order to verify our understanding of the observed phenomena. Currents from surface illumination are expected to be collected in the two outer chambers of the cell and the absence of such currents in the central chamber was verified by the laser-detuning dependence of the signals. Figure 4 shows the electrode current as a function of electrode voltage. Here the current magnitude is essentially symmetric and saturated. This confirms that all charges were collected and that no additional electron-collisional ionization occurred. In addition, we have maintained low currents (10^{-9} to 2×10^{-8} A) and charge densities to minimize space-charge effects.

Equation (1) predicts that the ion signal should scale as the square of the 3P-atom density. To test this we varied the laser power over two orders of magnitude, with the laser tuned to the wing of the D_2 line, and monitored the D_1 fluorescence signal I_1 and the ion signal. Here the D_1 signal is used as a relative measure of n_{3P}, since it is free of laser scatter and Rayleigh scattering and since $n_{3P_{1/2}}/n_{3P_{3/2}}$ is fixed for a given total Na density.[14] Figure 5 is a plot of the ion current i divided by I_1^2 vs I_1, where I_1 is equivalent to n_{3P}. The expected quadratic dependence (within $\sim 20\%$ as i varies over four orders of magnitude) is evident. A possible explanation for the small, systematic deviation from quadratic behavior which appears in Fig. 5 will be mentioned in the discussion section.

Figure 6 is a plot of i/n_{3P}^2 as a function of detuning near the D_2 line, where again I_1 was used to monitor n_{3P}. In this case it is especially important to monitor the D_1 fluorescence as a measure of n_{3P}, since the D_2 intensity
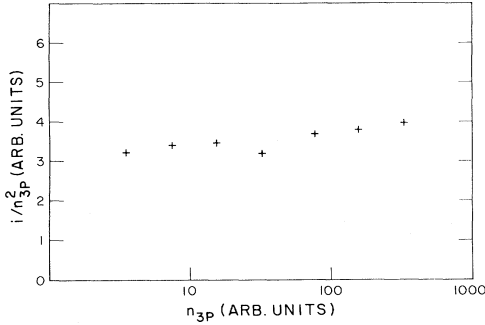
FIG. 5. Power dependence of i/n_{3P}^2 (plotted against n_{3P}). n_{3P} was varied by changing the laser power using a set of calibrated neutral density filters. D_1 fluorescence (which scales linearly with laser power) was used as a measure of n_{3P}. Background surface currents were eliminated by chopping the laser and using lock-in detection. Laser was detuned ~ 9.95 GHz to the blue of the D_2 line. [Na]$\sim 3.0 \times 10^{14}$ cm^{-3}. $V = -2.7$ V.

FIG. 6. i/n_{3P}^2 vs detuning from the D_2 line. D_1 fluorescence was used as a measure of n_{3P}. Background surface currents were eliminated by chopping the laser and using lock-in detection. [Na]$\sim 1.1 \times 10^{14}$ cm^{-3}. $V = -2.7$ V.

contains a large Rayleigh-scattering contribution whose escape probability changes with detuning (Refs. 14 and 15 contain more detailed discussions of these effects). As the detuning varies, i/n_{3P}^2 is expected to remain constant. This appears to be approximately true for $|\Delta| > 6$ GHz in Fig. 6, although at the largest detunings the signal-to-noise ratio becomes very poor. As the detuning is decreased below 6 GHz, a systematic effect appears, and i/n_{3P}^2 begins to increase dramatically, going far off scale for detunings less than 2 GHz. This behavior can be understood by realizing that ions are collected in the entire volume between $z = -0.635$ and $+0.635$ cm, whereas the fluorescence is collected from a thin volume of width
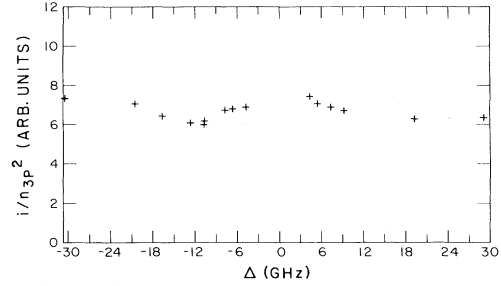
$\Delta z \sim 0.05$ cm located at $z = 0$ (see Fig. 2). The fluorescence at $z = 0$ is only a good measure of the average of n_{3P} throughout the ion detection volume if the attenuation of the laser from $z = -0.635$ to $+0.635$ cm is not too severe. For small detunings this is not the case; the excited atoms and ions are then produced primarily near the front edge of the volume ($z \sim -0.635$ cm) and $i/(I_1)^2$ increases. Beyond ~ 6 GHz the attenuation over the central chamber is < 0.2 at $n = 1.1 \times 10^{14}$ cm^{-3} and $i/(I_1)^2$ $\sim$ const (to within $\sim 20\%$).

We also verified that, as expected, i/n_{3P}^2 is independent of laser polarization, where (unpolarized) D_1 fluorescence was again used to monitor n_{3P}.

Absolute values for the AI rate coefficient were obtained by combining Eqs. (4) and (5) (x and z are in units of cm):

$$k_{AI} = i \left[e[n_{3P}(0,0,0)]^2 \int_{-0.317}^{0.317} dx [\phi_{ss}(x)]^2 \int_{-\infty}^{\infty} dy [Y(y)]^2 \int_{-0.635}^{0.635} dz [Z(z)]^2 \right]^{-1}. \tag{9}$$

In Table I we present our data and values of k_{AI} as obtained from Eq. (9). Uncertainties are discussed below.

The uncertainty in i is at most a few percent. $Z(z)$ is well known from measurements of the laser-beam attenuation, and $Y(y)$ was measured, as described previously, under the same cell and excitation conditions as the measurement of i. Thus both the y and z integrals in Eq. (9)

are estimated to be uncertain by less than $\sim 10\%$. Typically, $\int dy [Y(y)]^2 \sim 0.35$ cm and $\int dz [Z(z)]^2 \sim 1.29$ cm. The function $\phi_{ss}(x)$, applicable to this steady-state experiment, is bounded by the laser distribution $I(x)$ and the fundamental-mode distribution $n_0(x)$ [see Eq. (6) and Fig. 3]. Calculating $\phi_{ss}(x)$ as in Eqs. (7) and (8) including the first four even modes ($i = 0$, 2, 4, and 6) yields

TABLE I. Reduced experimental data.

[Na] (10^{14} cm^{-3})	Laser detuning (GHz)	T (K)	i (10^{-9} A)	Power absorbed $n_{3P}(0,0,0)$ (10^{11} cm^{-3})	Fluorescence calibration $n_{3P}(0,0,0)$ (10^{11} cm^{-3})	Excitation transfer $n_{3P}(0,0,0)$ (10^{11} cm^{-3})	k_{AI} (10^{-12} cm^3/s)	σ_{AI} (Å^2)
2.07	+ 10.6	637	6.30	2.02	2.25	2.71	5.43	0.502
	+ 7.7	637	10.5	2.45	2.77	3.16	5.99	0.553
5.47	+ 20.6	679	10.8	3.14	2.40	3.69	5.41	0.484
	− 19.2	679	8.10	2.64	2.13	3.47	5.42	0.485
							av 5.56	av 0.506
0.250	+ 4.3	578	1.7		1.25		4.30	0.417

$$\int_{-0.317}^{0.317} dx [\phi_{ss}(x)]^2 = 0.315$$

(in units of cm) with an estimated 10% uncertainty.

The uncertainty in $n_{3P}(0,0,0)$, obtained from each of the three methods discussed in Sec. III and in the appendixes, is between 20% and 39%. The main sources of these uncertainties are the "excitation fraction" K and $\phi(x)$ in the power absorbed method (Appendix A), $n_{3P}(0,0,0)_{\text{pulsed}}$ and $(I_{3P})_{\text{cw}}/(I_{3P})_{\text{pulsed}}$ in the fluorescence method, and k_{5S} in the excitation transfer method. Thus, the three methods can be considered statistically independent and we obtain the uncertainty σ in the weighted mean of $n_{3P}(0,0,0)$ from

$$\sigma = \left[\sum_i (1/\sigma_i^2) \right]^{-1/2}$$

(see Ref. 17), where the σ_i are the uncertainties estimated for each of the three methods. This yields $\sigma \cong 16\%$, and as $k_{\text{AI}} \propto [n_{3P}(0,0,0)]^{-2}$ this yields 32% uncertainty in k_{AI}, which then has an overall uncertainty of $\sim 37\%$.

The values of k_{AI} obtained from Eq. (9), using the weighted average of the three methods of determining $n_{3P}(0,0,0)$, are given in Table I for two Na densities and different detunings. These values are in good agreement and we therefore report the following result (in cm^3/s) for the rate coefficient:

$$k_{\text{AI}} = 5.6 \times 10^{-12} \; (\pm 37\%) \; . \tag{10}$$

Cross sections may be obtained from the rate coefficients using the definition $\sigma_{\text{AI}} \equiv k_{\text{AI}}/\bar{v}$ where $\bar{v}$ is the mean relative velocity of atoms in the vapor. These values are also given in Table I and we obtain (in Å^2)

$$\sigma_{\text{AI}} = 0.51 \; (\pm 37\%) \; . \tag{11}$$

Densities below 10^{14} cm^{-3} were not studied extensively, since under those conditions Γ_{eff} is not independent of density.[15] Nevertheless, to check that everything was behaving as expected, we did make one measurement at $n \sim 2.5 \times 10^{13}$ cm^{-3}. In this case we only measured $n_{3P}(0,0,0)$ by the fluorescence method, correcting the fluorescence for Γ_{eff} using the previously determined[15] density dependence of the fundamental-mode Γ_{eff}. We took $n_0(x)$ from van Trigt's[12] Doppler-regime fundamental-mode distribution and interpolated $\phi_{ss}(x)$ from this and $I(x)$, but we used the same $Y(y)$ that was measured at $n = 2 \times 10^{14}$ cm^{-3}. The rate coefficient, obtained in this manner and reported in Table I, is 4.3×10^{-12} cm^3/s which is in good agreement with our high-density results considering the uncertainty in this case is $\sim 75\%$. Owing to the large uncertainty, this result was not included in the averages of k_{AI} and σ_{AI} above, but is included here as further verification of our method.
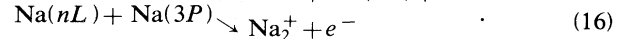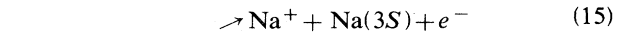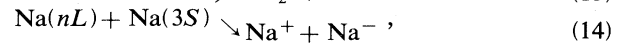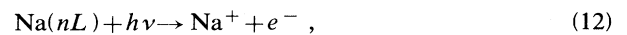
V. DISCUSSION

A. Pulsed-laser excitation

In the early stages of this experiment, we attempted to measure the associative ionization current following $3P$ excitation by a 5-ns pulse of D-line radiation from a N_2-laser pumped dye laser, since we already had developed a direct measure of the $3P$ density under these conditions.[11] We found, however, a very large ionization signal, of $\sim 10^{-10}$ C/pulse at $[\text{Na}] \cong 3 \times 10^{13}$ cm^{-3}. We attributed this to multiphoton ionization of $3P$ atoms in spatial regions where the laser field was enhanced by self-focusing. This is followed by collisional ionization by superelastic collisionally heated electrons as first suggested by Measures.[3] This self-focusing hypothesis was consistent with the results obtained tuning the laser slightly off resonance to both the red and blue, while fixing the $3P$ density (as measured by fluorescence). We observed a large detuning asymmetry in this ionization signal, which is consistent with the self-focusing that occurs only for detunings to the side of the line where the index of refraction increases with saturation. The ionization current was still excessive with detuning to the other side; we attribute this to residual multiphoton ionization and electron-collisional ionization. Thus, for the densities studied using pulsed excitation, we were unable to unambiguously separate the AI current from that produced by multiphoton ionization. As noted above, the experiment was then carried out with cw-laser excitation, at which low power (I) a much smaller $3P$ density, fewer superelastic electron-heating collisions, negligible self-focusing, and much less two-photon ionization of Na $3P$ atoms occurred, i.e., for small I the Na($3P$)+Na($3P$) ionization is proportional to I^2, two-photon ionization of $3P$ is proportional to I^3, and ionization by superelastically heated electrons to still higher powers in I.

B. Additional ionization mechanisms

In addition to process (1), several other mechanisms may produce ions even in this relatively weak, cw-laser excitation experiment. Higher nL states populated through process (2) may undergo photoionization, associative ionization, or Penning ionization:

$$\text{Na}(nL) + h\nu \rightarrow \text{Na}^+ + e^- \; , \tag{12}$$

$$\text{Na}(nL) + \text{Na}(3S) \begin{cases} \nearrow \text{Na}_2^+ + e^- & \tag{13} \\ \searrow \text{Na}^+ + \text{Na}^- & \tag{14} \end{cases}$$

$$\text{Na}(nL) + \text{Na}(3P) \begin{cases} \nearrow \text{Na}^+ + \text{Na}(3S) + e^- & \tag{15} \\ \searrow \text{Na}_2^+ + e^- & \tag{16} \end{cases}$$

Additionally, ionization by collisions with hot electrons

$$\text{Na}(3S, 3P, nL) + e^- \rightarrow \text{Na}^+ + 2e^- \; , \tag{17}$$
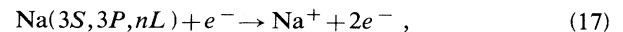
multiphoton ionization, and even radiation-assisted collisional ionization processes can occur. Since our collection system does not distinguish between atomic and molecular ions, all such processes should be considered.

From the rate equation governing process (2), which appears in Appendix C [see Eq. (C8)], we find

$$n_{nL} = k_{nL} n_{3P}^2 / \Gamma_{nL} \; , \tag{18}$$

where k_{nL} is the rate coefficient for process (2) and Γ_{nL} is the total radiative rate out of the level nL. (This equation is only valid if the various collisional rates out of the nL level are small compared to Γ_{nL}.) Using the rate coefficients $k_{4D}=2.46\times10^{-10}$ cm^3/s and $k_{5S}=1.63\times10^{-10}$ cm^3/s from Ref. 11, $\Gamma_{4D}=1.98\times10^7$ s^{-1} and $\Gamma_{5S}=1.26\times10^7$ s^{-1} from Refs. 4 and 18, and $n_{3P}(0,0,0)<3.5\times10^{11}$ cm^{-3} from Table I, we obtain n_{4D}, $n_{5S}<1.5\times10^6$ cm^{-3}. All other n_{nL}'s are even smaller (see Ref. 11). The photoionization (PI) current from process (12) is then given by $i_{PI}=e\sigma_{PI}I\int n_{4D}dV/(\hbar\omega)$, where I is the laser intensity, σ_{PI} the photoionization cross section, and $\hbar\omega$ the photon energy. For the above n_{4D}, our laser intensity of ~0.1 W/cm^2 and photoionization cross sections $\sigma_{PI}<10^{-16}$ cm^2 (Refs. 19—21), we obtain $i_{PI}<2\times10^{-12}$ A which is a negligible contribution to our observed currents (see Table I). This is also consistent with the observation that the current scales with the square of the laser power rather than with the cube.

Since n_{nL} scales as n_{3P}^2 [see Eq. (18)], currents produced by processes (15) and (16) should scale as n_{3P}^3. Figure 5 demonstrates that this is not the case, allowing us to rule out these processes as significant contributors to our observed currents. (The slight deviation from quadratic dependence which can be seen in Fig. 5 may be due to these processes but if so, the contribution to the observed current is less than 10% at the highest $3P$ densities.) From Eq. (18) we see that the ratio of current from process (15) to process (1) is

$$i_{(15)}/i_{(1)}=k_{(15)}n_{3P}n_{nL}/(k_{(1)}n_{3P}^2),$$

which even for the very large rate coefficients ($\sim10^{-8}$ cm^3/s) obtained by Chéret et al.$^{22-24}$ for the analogous process in Rb is ~0.01. Thus our data can shed no light on the magnitude of this rate coefficient, and process (15) does not interfere significantly with our measurement of k_1.

The ratio of current produced through process (13) relative to that through process (1) is

$$i_{(13)}/i_{(1)}=k_{(13)}n_{3S}n_{nL}/(k_{(1)}n_{3P}^2),$$

which in the worst (highest-n_{3S}) case in Table I with the n_{4D} given below Eq. (18) becomes $\sim10^{-2}(k_{(13)}/k_{(1)})$. Using a rate coefficient of $k_{(13)}=k_{AI}(4D)\sim8\times10^{-11}$ cm^3/s from Ref. 10 we obtain $i_{(13)}\sim10^{-9}$ Å which is $\sim10\%$ of our observed current. The data in Table I also put an upper limit on this possible contribution, as well as on process (14). n_{3P} is roughly constant in the data presented in Table I, while n_{3S} varies by a factor of ~2.5 for the more accurate data, or by a factor of ~20 if we include our less accurate $n\sim2.5\times10^{13}$ cm^{-3} measurement. No significant change in k_{AI} is observed, whereas any contribution from processes (13) or (14) would scale linearly with n_{3S}. Since many of the calibration factors that yield the final 37% uncertainty in k_{AI} are common to all measurements, this test puts an upper limit of $\sim15\%$ on the contribution of (13) and (14) to the current. The absence of any n_{3S} dependence to the observed current, within this accuracy, places an upper bound of $\sim2\times10^{-10}$ cm^3/s on $k_{AI}(4D)+k_{AI}(5S)$, which is con-

sistent with Kushawaha and Leventhal,[10] who measured $k_{AI}(4D)=7.8\times10^{-11}$ cm^3/s and $k_{AI}(5S)=3.3\times10^{-13}$ cm^3/s.

Penning and associative ionization involving two atoms in high-nL levels can be eliminated from consideration due to the small density of atoms in these levels and the dependence of the ion current on n_{3P}^4 for these processes. Laser-assisted and multiphoton processes are also negligible at the laser powers used here (<0.1 W/cm^2).

The electrons move, on the average, across half the cell width $W/2$. If the ionization cross section for $e^-+Na(nL)\rightarrow Na^++2e^-$ is σ_{nL}, then the ratio of secondary ionization current, due to this process (17), to primary current i is $\sum_{nL}\sigma_{nL}n_{nL}W/2$. For reasonable values, $n_{4D}+n_{5S}\sim3\times10^6$ cm^{-3}, $\sigma_{4D,5S}<10^{-13}$ cm^2 (Ref. 25), $n_{3P}\sim3\times10^{11}$ cm^{-3}, $\sigma_{3P}<10^{-14}$ cm^2, and $W/2\sim0.3$ cm, this ratio is completely negligible ($<10^{-3}$). Furthermore, these upper limits on the σ_{nL} apply to electrons with sufficient energy to ionize the $4D$ and $3P$ state (1 and 3 eV, respectively), while the probability of an electron-Na($3P$) superelastic collision before the electron reaches the cell wall is less than 0.1 (using superelastic collision rate coefficients $\sim10^{-7}$ cm^3/s from Ref. 26). Thus this energy can only be gained in the applied field, whereas saturation of i with V is seen in Fig. 4.

C. Comparisons

Several values of the Na($3P$)+ Na($3P$) AI rate coefficient have previously been published. The earliest of these appears to be that of Klyucharev et al.[8] who measured n_{3P} by absorption to higher levels. Their result $k_{AI}=(3.8\pm0.4)\times10^{-11}$ cm^3/s at $T\sim575$ K, is about seven times larger than our result and well outside the combined error bars. We do not fully understand the origin of this discrepancy, but we note that Klyucharev et al. have not discussed the spatial distribution of excited atoms in their analysis. Additionally, their ionization signals were complicated by a linear term in the pumping-lamp intensity that they attribute to surface emission of electrons.

Bearman and Leventhal[27] estimated the rate coefficient for process (1) at 10^{-10} cm^3/s from their earlier experimental data, but a later quantitative measurement by Kushawaha and Leventhal[10] yielded a rate coefficient of 1.3×10^{-12} cm^3/s at $T\sim500$ K. This value is about four times smaller than our result. Complications in the Kushawaha and Leventhal experiment include obtaining the excited-atom density from an absolute calibration of the fluorescence intensity. However, the most serious issue, as in all such experiments, is an unknown spatial distribution of excited atoms due to the laser-intensity distribution and radiation trapping effects, combined with possible nonuniformities in the ground-state atom density due to nonequilibrium conditions in their cell.

de Jong and van der Valk[9] obtained a cross section for process (1) of 5×10^{-18} cm^2, to within a factor of 2, using a crossed-beam apparatus. This is a factor of 10 below our result, but this might be explained on the basis of a temperature or velocity dependence of the cross section; i.e., the mean collision velocity in their experiment corre-

TABLE II. Comparison of experimental rate coefficients and cross sections for associative ionization of alkali-metal atoms.

Alkali metal	Collision partners	T (K)	k_{AI} (10^{-13} cm^3/s)	$\sigma_{AI} \equiv k_{AI}/\bar{v}$ (Å^2)	Reference
Cs	$6P+6P$	500		0.07 ± 0.05	29
		450		11 ± 3	30
		425	2.0 ± 0.2	0.054 ± 0.005	31
Rb	$5P+5P$	473	3.2 ± 0.4	0.066 ± 0.008	32
K	$4P+4P$	450	9 ± 2	0.13 ± 0.03	8
Na	$3P+3P$	575	380 ± 40	3.7 ± 0.4	8
		500		10	27
		Beam; $V_{rel}=3.8\times10^4$ cm/s	1.5	~0.05	9
		498	13	0.14	10
		~650	56	0.51	This work
Li	$2P+2P$	900		0.0005	34

sponds to a temperature of 78 K compared to ~650 K in our experiment. The lower σ_{AI} we observed at 580 K is consistent with this possibility, although not sufficiently accurate to draw a definite conclusion.

Kircz et al.[28] studied the polarization dependence of Na($3P$)-Na($3P$) AI in atomic beams and found significant differences in cross sections for collisions involving two $3P_{3/2}$ atoms in the $M=\frac{3}{2}$ sublevel as opposed to two atoms in the $M=\frac{1}{2}$ sublevel. Our experiment was carried out at relatively high temperatures, and in a cell where randomly distributed relative velocities and rapid collisional mixing cause our cross section to be an average over orientations and over hyperfine- and fine-structure levels. This may explain part of the discrepancy between our result and de Jong and van der Valk's since they excited specific M levels of the $3P_{3/2}$ state only.

Table II, which is similar to Table 1 of Ref. 9, but updated to include recent results, is a comparison of rate coefficients and cross sections for excited-atom—excited-atom AI of all the alkali metals. We are not aware of any calculations of these rate coefficients.

VI. CONCLUSIONS

We have measured the rate coefficient for AI due to the collision of two excited Na atoms. This has been done by a thorough analysis and measurements of the spatial distribution of excited atoms, combined with three essentially independent measurements of the total excited-atom density. This result is thus free of the systematic errors that have often arisen in such measurements from unsubstantiated assumptions regarding the volume and density of excited atoms. Furthermore, we have been careful to utilize low-power lasers and low excited-atom densities plus checks of power dependence to avoid many higher-order processes that also frequently lead to errors in this type of measurement.

The AI rate coefficient k_{AI} measured here is almost certainly due to crossings of Na$_2$ states arising from the Na($3P$)+ Na($3P$) separated atom limit with the ground state of Na$_2^+$, near its minimum at $R_e \cong 3.5$ Å. However, $\bar{v}_{12}\pi R_e^2 \cong 4\times10^{-10}$ cm^3 s^{-1} is a factor of 100 greater than the measured k_{AI}. This reduction can be attributed in

part to a statistical factor related to crossing by only a small portion of all the states arising from Na($3P$)+ Na($3P$), and in part to a probable activation energy associated with the energy of these crossings relative to the initial Na($3P$)+ Na($3P$) energy.

ACKNOWLEDGMENT

APPENDIX A: DETERMINATION OF $n_{3P}(0,0,0)$ FROM THE POWER ABSORBED

By setting the excited-atom-production rate equal to the radiative decay rate, we find that the total power absorbed from the laser beam P is given by

$$KP = \hbar\omega \int \int \int n_{3P}(x,y,z)\Gamma_N g(x,y,z)dx\, dy\, dz\ ,$$

(A1)

where $\hbar\omega$ is the photon energy, K is the fraction of power P removed from the laser beam that results in excitation, and $g(x,y,z)$ is the angle-averaged escape probability for radiation emitted at x,y,z. In the central chamber of the cell and near the laser axis, the geometry is well represented by an infinite slab[13] so that $g(x,y,z)$ reduces to $g(x)$. Taking Eq. (5) in (A1) then yields

$n_{3P}(0,0,0)$

$$= \frac{KP}{\hbar\omega} \left[\Gamma_N \int dy\, Y(y) \int dz\, Z(z) \int \phi(x)g(x)dx \right]^{-1}.$$

(A2)

Here $\int_{-\infty}^{\infty} dy\, Y(y)=0.54$ cm at $n=2.07\times10^{14}$ cm^{-3} and 0.48 cm at $n=5.47\times10^{14}$ cm^{-3} is known, within an estimated 8% from the measured $Y(y)$ (see Fig. 3). If a power P_0 is incident on the vapor, the power P removed from the laser beam in the central chamber (1.905 to 3.175 cm from the entrance window) is ($-k_v$ is in units of cm)

$$P = P_0(e^{-k_v\times(1.905)} - e^{-k_v\times(3.175)})\ ,$$

(A3)

where k_v is known from the laser attenuation on versus

off resonance. (Typically $P/P_0 \sim 0.1-0.2.$) Overall uncertainty in P, primarily from uncertainty in calibrating P_0, is estimated at 10%. From knowledge of k_v, $\int Z(z)dz$ is typically equal to 1.28 cm and is known within an estimated 5% uncertainty.

Each slab-diffusion eigenfunction $n_i(x)$ [see Eq. (6)] decays into itself such that

$$\int n_i(x)g(x)dx = g_i \int n_i(x)dx , \qquad (A4)$$

where $g_i \Gamma_N \equiv \beta_i$ is the effective decay rate for the ith mode. Thus when $\phi(x)$ is expressed as a sum of eigenfunctions, as in Eq. (8), we obtain

$$\int \phi(x)g(x)dx = \sum_i a_i \beta_i^{-1} \int n_i(x)g(x)dx \Big/ \sum_i a_i \beta_i^{-1} n_i(0)$$

$$= \sum_i a_i \beta_i^{-1} g_i \int n_i(x)dx \Big/ \sum_i a_i \beta_i^{-1} n_i(0) ,$$

$$(A5)$$

where (A4) was used in the final step. If $\phi(x)$ consisted entirely of fundamental mode ($a_0 = 1$, $a_{i>0} = 0$), (A5) with $n_0(x)$ from Ref. 12 would yield

$$\Gamma_N \int_{-l}^{l} \phi(x)g(x)dx = \Gamma_n g_0 \int_{-l}^{l} n_0(x)dx / n_0(0)$$

$$= (1.54l)\Gamma_N g_0 ,$$

where $2l$ is the slab thickness (0.635 cm). Here $\Gamma_N g_0$ is the known fundamental-mode decay rate $\Gamma_{\rm eff}^{(0)}$ of Holstein and van Trigt, which has been verified for Na in Ref. 13. Using the more accurate $\phi_{\rm ss}(x)$, by including the $i = 0$, 2, 4, and 6 terms in Eq. (A5) yields a 21% smaller effective radiative escape rate

$$\Gamma_N \int \phi_{\rm ss}(x)g(x)dx = 0.79(1.54l)\Gamma_N g_0 . \qquad (A6)$$

This correction results because the actual $\phi(x)$ is concentrated further from the sapphire rods, where radiative escape is slower. The uncertainty in this (A6) evaluation of $\Gamma_{\rm eff} = g\Gamma_N$ is estimated at $\sim 10\%$, due to differences between ideal-slab and the actual experimental geometry, and uncertainty in g_0.

The factor K in expression (A1) must be considered carefully. Since the laser is tuned slightly off resonance, we can consider it to populate a "virtual" $3P$ level at that frequency.[35,36,14] (This interaction is more accurately described as a coherence, but for our purposes the virtual-level picture is adequate.) Atoms in the virtual level either radiate photons at the laser frequency, at a rate Γ_N, and return to the ground state (Rayleigh scattering) or they undergo line-broadening collisions, with a rate $\Gamma_{\rm br}$, which can leave them in the "real" excited state that fluoresces at the atomic frequency. For the densities of our experiment, the rates for these two processes are of the same order of magnitude, but radiation trapping of the collisionally induced fluorescence causes the effective lifetime $1/\Gamma_{\rm eff}$ of the real excitation to be 2 to 3 orders of magnitude greater than $1/\Gamma_N$. Thus the real excited-state population greatly exceeds the virtual-state population and therefore only those atoms in the real state contribute significantly to the associative ionization and excitation transfer signals. The factor K is therefore the fraction of photons absorbed

from the beam that result in real excitation. If the laser were far from resonance, K would be given by $\Gamma_{\rm br}/(\Gamma_N + \Gamma_{\rm br})$ (Ref. 35) where $\Gamma_{\rm br}$ is the self-broadening rate for the Na D_2 line (see Ref. 15). For smaller detunings, a fraction (f) of Rayleigh-scattered light (which for emission at right angles to the laser beam is redistributed in frequency over a Doppler profile) is reabsorbed before escaping the cell and thus results in additional real excitation. K is therefore given by

$$K = \frac{\Gamma_{\rm br} + f\Gamma_N}{\Gamma_{\rm br} + \Gamma_N} . \qquad (A7)$$

f was obtained by measuring the spectrally resolved Rayleigh, D_2- and D_1-line intensities, with the laser in the optically thin wing of the D_2 line, and comparing these to the D_1 and unresolved Rayleigh plus D_2-line intensities measured with the laser frequency set to the frequency used to measure $k_{\rm AI}$ (see Ref. 15). Typically $f \sim 0.1$. K can then be found from (A7) and previous measurements of $\Gamma_{\rm br}$ vs Na density.[15] We estimate that K, obtained as described here and typically in the range 0.6–0.85, is uncertain by no more than 10%. Values of $n_{3P}(0,0,0)$ calculated from Eq. (A2) are listed in Table I.

Assuming no correlations among the systematic errors exist, we may combine the uncertainties of the individual terms in quadrature and arrive at a total uncertainty of $\sim 20\%$ in $n_{3P}(0,0,0)$ obtained by this method.

APPENDIX B: DETERMINATION OF $n_{3P}(0,0,0)$ FROM FLUORESCENCE CALIBRATION

In Ref. 11 we describe measurements of the $3P$-atom density, following pulsed excitation of the $3P_{3/2}$ state, by monitoring the change in the transmission of a weak cw probe laser also tuned near the D_2 frequency. (The cw transmission depends upon $n_{3P_{3/2}} - (g/g^*)n_{3S_{1/2}}$, where g and g^* are the lower and upper statistical weights, respectively.) The quantity actually measured by this technique is $\int_{-l}^{l} dx\, \phi(x)n_{3P}(0,0,0)$, where $2l$ is the slab thickness of 0.635 cm. However, since this measurement was made in the late time following pulsed excitation, $\phi(x)$ is unambiguously given by $n_0(x)$ [see Eq. (6)] which is accurately known.[15]

Under the same conditions as this absolute measurement of $n_{3P}(0,0,0)$, including the same time after the excitation pulse, we measured the D_1- and D_2-line fluorescence. The imaging was such that we collected light from a thin vertical strip, of 5-mm height, at $z = 0$ (i.e., from $y = -0.25$ to 0.25 cm in Fig. 3). Switching to cw excitation with the same laser-beam geometry, we then measured the D_1 and D_2 fluorescence from the same geometrical volume. In the pulsed case, calibrated neutral density filters were used to attenuate the fluorescence. The ratio of $3P$ fluorescence signals with cw- and pulsed-laser excitation is then given by (y is in units of cm)

$$\frac{(I_{3P})_{\text{cw}}}{(I_{3P})_{\text{pulsed}}} = \frac{[n_{3P}(0,0,0)]_{\text{cw}}\left[\int_{-l}^{l}dx\,\phi(x)P(x)\right]_{\text{cw}}\left[\int_{-0.25}^{0.25}dy\,Y(y)\right]_{\text{cw}}}{[n_{3P}(0,0,0)]_{\text{pulsed}}\left[\int_{-l}^{l}dx\,\phi(x)P(x)\right]_{\text{pulsed}}\left[\int_{-0.25}^{0.25}dy\,Y(y)\right]_{\text{pulsed}}} ,$$ (B1)

where factors such as detection solid angles, detection system efficiencies, and photon energies cancel in the ratio. The factor $P(x)$ is the probability of photon escape in the detection direction. Taking $\phi(x)_{\text{pulsed}} = n_0(x)$ and $\phi(x)_{\text{cw}}$ from Eq. (8), and noting that $P_i(x)$ for each mode is proportional to $g_i(x)$ (see Appendix A) we obtain

$$\frac{\left[\int_{-l}^{l}dx\,\phi(x)P(x)\right]_{\text{cw}}}{\left[\int_{-l}^{l}dx\,\phi(x)P(x)\right]_{\text{pulsed}}} = \frac{\sum_i a_i\beta_i^{-1}\int_{-l}^{l}dx\,n_i(x)g_i(x)\left[\sum_i a_i\beta_i^{-1}n_i(0)\right]^{-1}}{\int_{-l}^{l}dx\frac{n_0(x)}{n_0(0)}g_0(x)}$$

$$= \frac{\sum_i a_i\beta_i^{-1}g_i\int_{-l}^{l}n_i(x)dx\left[\sum_i a_i\beta_i^{-1}n_i(0)\right]^{-1}}{g_0[n_0(0)]^{-1}\int_{-l}^{l}n_0(x)dx} .$$ (B2)

The final expression in (B2) was shown in Appendix A to equal 0.79. The ratio of the y integrals in Eq. (B1) is very nearly 1, since significant differences in $Y(y)_{\text{cw}}$ and $Y(y)_{\text{pulsed}}$ only occur in regions outside the observed region ($|y| > 0.25$ cm). Thus (B1) reduces to

$$\frac{(I_{3P})_{\text{cw}}}{(I_{3P})_{\text{pulsed}}} = 0.79\frac{[n_{3P}(0,0,0)]_{\text{cw}}}{[n_{3P}(0,0,0)]_{\text{pulsed}}} .$$

Interference from Rayleigh scattering in the cw-laser-excitation case requires that the ratio $(I_{3P})_{\text{cw}}/(I_{3P})_{\text{pulsed}}$ be determined from the transferred (D_1) component. This introduces no serious complication since the $3P_{3/2}$ and $3P_{1/2}$ densities are close to their statistical ratio and small corrections are known from the known excitation transfer rate coefficient[13] and measurements of the D_1 to D_2 intensity ratio in the pulsed-laser-excitation experiment.

Uncertainties in $[n_{3P}(0,0,0)]_{\text{cw}}$ from Eq. (B1) are $\sim 10\%$ in the x integral ratio, $\sim 5\%$ in the y integral ratio, and $\sim 20\%$ in $[n_{3P}(0,0,0)]_{\text{pulsed}}$ (see Ref. 11). Time con-

straints did not permit repetition of the signal calibration procedure, which was later found to have some minor inconsistencies. Thus we must assign an uncertainty of $\sim 30\%$ to $(I_{3P})_{\text{cw}}/(I_{3P})_{\text{pulsed}}$ for this experiment although in principle this quantity could be obtained far more accurately.

Combining uncertainties in quadrature, we arrive at an overall uncertainty of $\sim 38\%$ in $n_{3P}(0,0,0)$ determined by this technique.

APPENDIX C: DETERMINATION OF $n_{3P}(0,0,0)$ FROM THE $3P + 3P \rightarrow 3S + 5S$ EXCITATION TRANSFER

As in the fluorescence calibration procedure (Appendix B), we observed fluorescence from the thin, 5-mm-high strip at $z = 0$. The $3P \rightarrow 3S$ fluorescence intensity I_{3P} emitted in the x direction into the detection solid angle $d\Omega$ from the volume defined by this strip is given by (y is in units of cm)

$$I_{3P} = \frac{S_{3P}}{\epsilon_{3P}} = \hbar\omega_{3P}\frac{d\Omega}{4\pi}\int_{-l}^{l}dx\int_{-0.25}^{0.25}dy\sum_J n_{3P_J}(x,y,0)\Gamma_{3P_J\rightarrow 3S}P_{3P_J\rightarrow 3S}(x,y,0) .$$ (C1)

In this expression S_{3P} is the photomultiplier current, ϵ_{3P} is the detection system sensitivity at the $3P \rightarrow 3S$ wavelength, $\hbar\omega_{3P}$ is the photon energy, $2l = 0.635$ cm is the cell width in the x direction, $\Gamma_{3P_J\rightarrow 3S}$ is the natural radiative rate for the $3P_J$ fine-structure components $(\Gamma_{3P_{1/2}} = \Gamma_{3P_{3/2}} = 6.3\times 10^7$ s$^{-1})$, and $P_{3P_J\rightarrow 3S}(x,y,0)$ is the position-dependent, photon escape probability in the detection direction. Since we used the density region where trapping is dominated by the impact-broadened Lorentzian line wing, $P_{3P_J\rightarrow 3S}(x,y,0)$ is given, from the Holstein theory, by

$$P_{3P_J\rightarrow 3S}(x,y,0) = [\pi k_p(J)(l-x)]^{-1/2} ,$$ (C2)

where

$$k_P(J) = \frac{\lambda^2}{2\pi}\frac{(2J+1)}{2}\frac{\Gamma_N n}{\Gamma_{\text{br}}(J)} .$$ (C3)

Measurements of $Y(y)$ have shown[15] that the $3P_{1/2}$ and $3P_{3/2}$ population distributions can both be described by the same function shown in Fig. 3, as expected in this pressure regime of almost complete $3P_J$ collisional mixing. Introducing (C2), (C3), and (5) into (C1) yields (y is in units of cm)

$$I_{3P} = \frac{S_{3P}}{\epsilon_{3P}} = \hbar\omega_{3P} \frac{d\Omega}{4\pi} \Gamma_{3P\to 3S} \sum_J \frac{n_{3P_J}(0,0,0)}{[k_p(J)\pi]^{1/2}} \int_{-0.25}^{0.25} dy\, Y(y) \int_{-l}^{l} dx\, \frac{\phi(x)}{(l-x)^{1/2}} \; . \tag{C4}$$

Taking $\Gamma_{br} \equiv k_{br} n$ from the calculation of Ref. 37 (which was verified in Ref. 15) yields $[\pi k_p(\frac{3}{2})]^{1/2}/1.11 = [\pi k_p(\frac{1}{2})]^{1/2} = 609 \text{ cm}^{-1/2}$. Combining this with

$$\frac{I_{D_1}}{I_{D_2}} = \left[\frac{k_p(\frac{3}{2})}{k_p(\frac{1}{2})} \right]^{1/2} \frac{n_{3P_{1/2}}}{n_{3P_{3/2}}} \tag{C5}$$

then results in (in $\text{cm}^{1/2}$)

$$\sum_J \frac{n_{3P_J}(0,0,0)}{[\pi k_p(J)]^{1/2}} = \frac{n_{3P}(0,0,0)}{609} \frac{I_{D_1} + I_{D_2}}{I_{D_1} + 1.11 I_{D_2}} \; . \tag{C6}$$

In a similar fashion we obtain an expression for the $5S \to 3P$ fluorescence (y is in units of cm)

$$I_{5S} = S_{5S}/\epsilon_{5S} = \hbar\omega_{5S} \frac{d\Omega}{4\pi} \Gamma_{5S\to 3P} \int_{-l}^{l} dx \int_{-0.25}^{0.25} dy\, n_{5S}(x,y,0) \; , \tag{C7}$$

where there is no trapping factor for the $5S \to 3P$ photons. The $5S$ level is populated through process (2), so that

$$\dot{n}_{5S} = 0 = k_{5S}[n_{3P}(x,y,z)]^2 - \Gamma_{5S} n_{5S}(x,y,z) \; , \tag{C8}$$

where k_{5S} is the $3P + 3P \to 5S + 3S$ rate coefficient and Γ_{5S} is the total radiative rate out of the $5S$ level. The ratio I_{5S}/I_{3P} from (C7) divided by (C4) may be solved for $n_{3P}(0,0,0)$; with the use of (C6) in (C4) and (C8) in (C7) this yields (in $\text{cm}^{1/2}$) (y is in units of cm)

$$n_{3P}(0,0,0) = \frac{S_{5S}}{S_{3P}} \frac{\epsilon_{3P}}{\epsilon_{5S}} \frac{\omega_{3P}}{\omega_{5S}} \frac{\Gamma_{3P\to 3S}}{\Gamma_{5S\to 3P}} \frac{\Gamma_{5S}}{k_{5S}} \frac{\int_{-0.25}^{0.25} dy\, Y(y)}{\int_{-0.25}^{0.25} dy\, [Y(y)]^2} \frac{\int_{-l}^{l} dx\, \phi(x)/(l-x)^{1/2}}{\left[\int_{-l}^{l} dx\, [\phi(x)]^2 \right] \times 609} \frac{I_{D_1} + I_{D_2}}{I_{D_1} + 1.11 I_{D_2}} \; . \tag{C9}$$

The ratio of the y integrals, from the measured $Y(y)$ such as that shown in Fig. 3, is ~ 1.2 with $\sim 5\%$ uncertainty. The ratio of the x integrals is $\sim 2.64 \text{ cm}^{-1/2}$ with an uncertainty of $\sim 8\%$, using the $\phi_{ss}(x)$ of Eq. (8). The term $(I_{D_1} + I_{D_2})/(I_{D_1} + 1.11 I_{D_2})$ is near 0.93 and known to $\sim 3\%$. The signal ratio S_{5S}/S_{3P} is uncertain by $< 10\%$, and the detection efficiency ratio, which was obtained using a calibrated tungsten lamp, is uncertain by $\sim 5\%$ (see Ref. 14). The branching ratio $\Gamma_{5S}/\Gamma_{5S\to 3P} = 1.75$ is uncertain by $< 10\%$. The main uncertainty in this method is k_{5S}, which is known to only $\pm 35\%$ (see Ref. 11). Thus, by combining uncertainties in quadrature, we arrive at the overall uncertainty of $\sim 39\%$ for this determination of $n_{3P}(0,0,0)$.

*Present address: Physics Department, Princeton University, Princeton, NJ 08540.

†Present address: Quantum Physics Division, National Bureau of Standards, Boulder, Colorado 80309.

[1]T. B. Lucatorto and T. J. McIlrath, Phys. Rev. Lett. 37, 428 (1976).

[2]C. H. Skinner, J. Phys. B 13, 55 (1980).

[3]R. M. Measures, J. Appl. Phys. 48, 2673 (1977).

[4]W. L. Wiese, M. W. Smith, and B. M. Miles, Atomic Transition Probabilities (U. S. GPO, Washington, D. C., 1969), Vol. II.

[5]J. N. Bardsley, B. R. Junker, and D. W. Norcross, Chem. Phys. Lett. 37, 502 (1976).

[6]V. S. Kushawaha and J. J. Leventhal, Phys. Rev. A 25, 570 (1982).

[7]D. J. Krebs and L. D. Schearer, J. Chem. Phys. 75, 3340 (1981).

[8]A. Klyucharev, V. Sepman, and V. Vuinovich, Opt. Spektrosk. 42, 588 (1977) [Opt. Spectrosc. (USSR) 42, 336 (1977)].

[9]A. de Jong and F. van der Valk, J. Phys. B 12, L561 (1979).

[10]V. S. Kushawaha and J. J. Leventhal, Phys. Rev. A 22, 2468 (1980); 25, 346 (1982).

[11]J. Huennekens and A. Gallagher, Phys. Rev. A 27, 771 (1983).

[12]C. van Trigt, Phys. Rev. 181, 97 (1969).

[13]J. Huennekens and A. Gallagher, Phys. Rev. A 27, 1851 (1983).

[14]J. Huennekens, Ph.D. thesis, University of Colorado, 1982 (unpublished).

[15]J. Huennekens and A. Gallagher, Phys. Rev. A 28, 238 (1983).

[16]T. Holstein, Phys. Rev. 72, 1212 (1947); 83, 1159 (1951).

[17]P. R. Bevington, Data Reduction and Error Analysis for the Physical Sciences (McGraw-Hill, New York, 1969).

[18]E. M. Anderson and V. A. Zilitis, Opt. Spektrosk. 16, 177 (1964) [Opt. Spectrosc. (USSR) 16, 99 (1964)].

[19]M. Aymar, E. Luc Koenig, and F. Combet Farnoux, J. Phys. B 9, 1279 (1976).

[20]M. Aymar, J. Phys. B 11, 1413 (1978).

[21]A. V. Smith, J. E. M. Goldsmith, D. E. Nitz, and S. J. Smith, Phys. Rev. A 22, 577 (1980).

[22]M. Chéret, A. Spielfiedel, R. Durand, and R. Deloche, J. Phys. B 14, 3953 (1981).

[23]M. Chéret, W. Lindinger, L. Barbier, and R. Deloche, Chem. Phys. Lett. **88**, 229 (1982).

[24]M. Chéret, L. Barbier, W. Lindinger, and R. Deloche, J. Phys. B **15**, 3463 (1982).

[25]I. C. Percival, Nucl. Fusion **6**, 182 (1966).

[26]D. H. Crandall, G. H. Dunn, A. Gallagher, D. G. Hummer, C. V. Kunasz, D. Leep, and P. O. Taylor, Astrophys. J. **191**, 789 (1974).

[27]G. H. Bearman and J. J. Leventhal, Phys. Rev. Lett. **41**, 1227 (1978).

[28]J. G. Kircz, R. Morgenstern, and G. Nienhuis, Phys. Rev. Lett. **48**, 610 (1982).

[29]G. Alfredo and A. Kniazzch, Bull. Am. Phys. Soc. **11**, 634 (1966).

[30]A. N. Klyucharev and N. S. Ryazanov, Opt. Spektrosk. **33**, 425 (1972) [Opt. Spectrosc. (USSR) **33**, 230 (1972)].

[31]B. V. Dobrolezh, A. N. Klyucharev, and V. Yu. Sepman, Opt. Spetrosk. **38**, 1090 (1975) [Opt. Spectrosc. (USSR) **38**, 630 (1975)].

[32]V. M. Borodin, A. N. Klyucharev, and V. Yu. Sepman, Opt. Spektrosk. **39**, 407 (1975) [Opt. Spectrosc. (USSR) **39**, 231 (1975)].

[33]A. Klyucharev, V. Sepman, and V. Vujnovic, J. Phys. B **10**, 715 (1977).

[34]A. von Hellfeld, J. Caddick, and J. Weiner, Phys. Rev. Lett. **40**, 1370 (1978).

[35]D. L. Huber, Phys. Rev. **170**, 418 (1968); **178**, 93 (1969).

[36]J. L. Carlsten, A. Szöke, and M. G. Raymer, Phys. Rev. A **15**, 1029 (1977).

[37]C. G. Carrington, D. N. Stacey, and J. Cooper, J. Phys. B **6**, 417 (1973).